Acoustic Flight Test of the Joby Aviation Advanced Air Mobility Prototype Vehicle

Kyle A. Pascioni*
NASA Langley Research Center, Hampton, VA, 23681, USA

Michael E. Watts†, Mary L. Houston‡
Analytical Mechanics Associates, Inc., Hampton, VA, 23681, USA

Andrew H. Lind§
NASA Langley Research Center, Hampton, VA, 23681, USA

James H. Stephenson†
US Army Combat Capabilities Development Command Aviation & Missile Center, Hampton, VA, 23681, USA

Jeremy J. Bain¶
Joby Aviation, Santa Cruz, CA, 95060, USA

An acoustic flight test was performed on the Joby Aviation preproduction all-electric vertical takeoff and landing prototype. With the design intent of carrying a pilot and four passengers a maximum range of 150 miles, this vehicle utilizes distributed propulsion and vectored thrust via six tilting propellers. As part of the Advanced Air Mobility (AAM) National Campaign, this is the first full-scale AAM aircraft tested by NASA over representative conditions for all phases of a typical mission profile. A 58-channel distributed microphone array was used to acquire acoustic measurements on more than 100 test points (31 unique conditions). The measurements were postprocessed with synchronously sampled vehicle position and state data to form ground noise contours of departures and approaches at various flight path angles and accelerations. Comparing ground areas of 65 dBA isolines, approaches consistently exhibit higher noise levels relative to departures. Directivity maps were generated for constant airspeed level flyovers. Examples comparing the differences between a semithrust-borne and full wing-borne mode are given, with full wing-borne mode representing the quietest phase of the flight envelope tested. Measurements for hover in and out of ground effect are given and found to have 2 to 5 dB variation over a single run, and more significant variation between back-to-back runs. Finally, initial analysis of acoustic symmetry about the longitudinal vehicle axis and repeatability over several test days are presented.

*Research Aerospace Engineer, Aeroacoustics Branch
†Acoustics Subject Matter Expert
‡Acoustics Data Analyst
§Research Aerospace Engineer, Aeroacoustics Branch, Member AIAA
¶Aeroacoustics and CFD Lead, Member AIAA

Nomenclature

a_∞	= $\mathrm{d}V_\infty/\mathrm{d}t$, Acceleration based on true airspeed [g]
$L_{A,\max}$	= Integrated maximum A-weighted sound pressure level [dBA re. 20 μPa]
L	= Integrated unweighted sound pressure level [dB re. 20 μPa]
L_A	= Integrated A-weighted sound pressure level [dBA re. 20 μPa]
M_t	= Propeller tip Mach number, [-]
V_w	= Wind velocity [kt]
V_∞	= True airspeed [kt]
(x, y, z)	= Local coordinate system re. microphone 17
γ	= Flight path angle [deg.]
θ	= Azimuthal angle [deg.]
ϕ	= Elevation angle [deg.]
θ_N	= Nacelle angle [deg.]
θ_b	= Propeller blade pitch [deg.]
Ω	= Propeller rotation rate [RPM]
SPL	= Sound pressure level, [dB/Hz re. 20 μPa]

Symbols:

$\overline{(\cdot)}$	Averaged quantity over a flight event

I. Introduction

Advanced Air Mobility (AAM) is a new and imminent sector in aviation primed to thrive in the coming years. In addition to air traffic management, autonomy, and safety, noise has been regarded as a major obstacle identified by the NASA Aeronautics Research Mission Directorate Strategic Implementation Plan.[1] To succeed, vehicles operating in close proximity to communities and urban cityscapes must not significantly increase noise pollution. Typical noise emission levels and their operational and configurational dependencies, however, are not well understood at this time. With that in mind, the NASA Advanced Air Mobility Project has initiated the AAM National Campaign[2] to partner with industry in an effort to aid in the success of this emerging market. The AAM National Campaign is a multiyear effort featuring flight test activities and 'scenarios' designed to address many of the anticipated challenges. One scenario is dedicated to noise evaluation and was the focus of the National Campaign Developmental Test (NC-DT), conducted in the summer of 2021 with partner company Joby Aviation[3] at their Electric Flight Base near Big Sur, CA. Acoustic measurements were acquired on the Joby preproduction prototype to help understand the noise source mechanisms, expected noise levels, and sound character of this new vehicle class.

Experimental research into aeroacoustic sources of multirotor/distributed propulsion vehicles has grown dramatically over the last several years.[4–7] While the small geometric scales of Unmanned Aerial Systems (UAS) lend nicely to full-scale measurements conducted in anechoic chambers or wind tunnels, full-scale passenger carrying aircraft are most often not realizable in the confines of a test facility. With AAM still in its infancy, the lack of acoustic measurements on full-scale aircraft inhibits the ability to extend aeroacoustic research beyond what is known on small-scale multirotor aircraft or conventional rotorcraft. The measurement effort reported in this paper aims to address this deficiency. Rizzi et al.[8] have summarized and identified knowledge gaps and provided recommendations on what should be investigated for Urban Air Mobility (UAM) noise, UAM being a subset of AAM. Full-scale acoustic measurements are noted to be a necessity to better understand the dominant source mechanisms and assess community impact. Furthermore, comparison and validation of noise prediction tools are in demand to reduce uncertainty and better understand simplifying assumptions.

This paper will provide an overview of the first NASA acoustic flight test with a full-scale AAM industry partner aircraft. Prior to the test, NASA and Joby Aviation designed a test matrix that included flight conditions representative of all phases of a typical mission profile. These test points and flight paths will be discussed. In addition to the Joby Aviation prototype electric Vertical Takeoff and Landing (eVTOL) aircraft[9] used in the test, instrumentation and measurement methodologies will be described. The microphone array was designed to characterize all phases of flight within the current operating envelope of the vehicle. Similar

to previous rotorcraft flight test campaigns, which aided in delivering generic guidance to conventional rotorcraft pilots on how to 'fly neighborly' within their operational envelope,[10] a distributed microphone array is utilized to measure ground noise footprints of near-ground (in this case, near-vertiport) operations. Additionally, directivity over large emission angle ranges of level flyovers, including both semithrust-borne flight and full wing-borne flight (the latter representing a cruise condition) are gathered using a nested linear subarray. Repeatability of these directivity maps is also presented using test points executed over multiple days. A semicircular subarray also enabled inspection of typical hover levels both in ground effect (HIGE) and out of ground effect (HOGE). While future publications on this dataset are expected, examples of each measurement type will be given here. Acoustic symmetry, which was assumed during the array design process, is validated for the pertinent flight conditions.

II. Vehicle Overview

Joby Aviation has been developing an all-electric vertical takeoff and landing aircraft that it intends to operate as part of a fast, quiet, and convenient air taxi service beginning in 2024. Joby first flew subscale flights in 2015 and its first full-scale prototype in 2017. The preproduction prototype shown in Figure 1 has been undergoing flight tests since 2019. It is designed for high-density operations near residences and workplaces, where acoustics is of high importance.[9,11] For this test, the aircraft was unmanned and remotely piloted, near its maximum gross weight, and outfitted with a recently upgraded faired landing gear.

The propellers were designed with five blades and high solidity to allow for lower tip speeds than are possible for conventional helicopters.[9] Details of the aircraft design concept and evolution can be found in Stoll et al.[12] Inspired by groundbreaking work on the experimental VAAC Harrier VTOL research platform[13] and later the F-35, the Joby aircraft employs a control strategy referred to as "unified flight control." The aircraft is controlled by a right sidestick and a throttle-like inceptor on the left. The sidestick controls the vertical axis, bank angle, and roll rate, and the left-hand inceptor controls longitudinal acceleration. The fly-by-wire control system individually adjusts each propeller's tilt angle, rotational speed, and blade pitch to achieve the desired trim state.

Figure 1. The Joby Aviation preproduction prototype vehicle (source: NASA and Joby Aviation).

III. Flight Test Setup

III.A. Array Layout and Flight Paths

The microphone array spanned a ground area of approximately 2,300 ft by 1,000 ft parallel and perpendicular to the main flight paths, respectively. Locations of individual microphones were designed to support acoustic

measurements of the aircract along two main flight paths as shown in Fig. 2: a departure/approach path and a level flyover path. Both flight paths were necessary given the surrounding terrain constraints and desire to fly at low altitudes to maximize emission angle coverage. For many test points, acoustic symmetry about the longitudinal vehicle axis was assumed to increase the lateral extent of the measurements. For example, the southern flight path skirts the bottom of the array with the majority of microphone stations north of this path. This off-centered path will allow ground noise contours to cover up to 700 ft sideline. The few microphones that are south of this path were intended to assess symmetry (which will be discussed in Section VI), and to the extent possible, have a microphone at a similar elevation angle for direct comparisons. Similarly, the northern flight path was biased to the northern edge of the array to avoid terrain and overflight of ground facilities. Measurements, which were acquired using this path, were mostly reserved for directivity mapping while the vehicle maintained a fixed nominal state, i.e., a constant true airspeed in level flight.

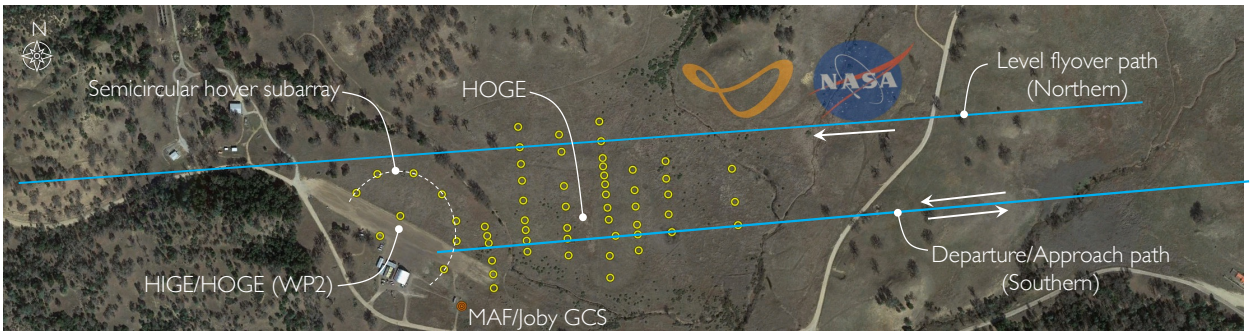

Figure 2. Overhead view of the hover locations and two main flight paths at Joby's Electric Flight Base. The yellow circles denote individual microphone stations.

Another feature of the layout was a seven channel semicircular subarray centered about the HIGE/HOGE ground point (WP2) to provide 180° azimuth coverage. A heading change for these test points provided full azimuth coverage at the particular elevation angle. Given the location of this subarray, these stations were also utilized when building the ground noise contours and provided insight into levels within 300 ft of the takeoff/landing point.

Figure 3 provides the microphone station numbering and local coordinate system that will be referenced in this paper. Locations of the ground weather stations and LiDAR vertical wind profiler, which will be discussed in the next section, are also shown. With the LiDAR units in close proximity to each of the two main flight paths, the ground-based weather stations were dispersed about the rest of the array. The contour in Fig. 3 is an interpolated surveyed height of each microphone station relative to station 17. To minimize terrain effects on the received acoustic signals, the ideal test site should be flat and free of hills, valleys, or tall vegetation. There are a few features of this test site that do not meet that criteria, particularly, the relatively steep elevation changes near stations 17 and 32 and the surrounding hills not captured in Fig. 3. Currently, the terrain effect has not been characterized. Note that there is also a gradual slope from left to right across the full array span. However, given the fact that ground elevation changes by only 25 ft over approximately 2,300 ft, no measurable issues are expected. Rustling vegetation was found to increase high-frequency background noise in preliminary measurements, even during low winds. To reduce this and to ensure line-of-sight, the field was cleared to ground level ±10 ft on all sides of the microphones.

III.B. Instrumentation

The acoustic data were acquired using a 58 channel distributed microphone array. Each channel employed a 1/2 inch prepolarized microphone (GRAS 67AX) flush mounted by the manufacturer to a 15 inch circular ground board. The preamplifiers were powered by 0.4 mA constant current supplied by a second generation Wireless Acoustic Measurement System (WAMS2) unit. The WAMS2 was designed and fabricated in-house at the NASA Langley Research Center. Each WAMS2 unit was powered by a 5 Ah battery (approximately 16 hour run time) pulling at most 3 W during active use. The individual units have an integrated circuit for data acquisition (Texas Instruments, Type ADS127L01) with a single channel 24 bit analog to digital delta-sigma converter for built-in antialiasing. The data were recorded and digitized at 25.0 kS/s and streamed to a 1 GB industrial grade single level cell SD card. An internal GPS unit was used to append Universal

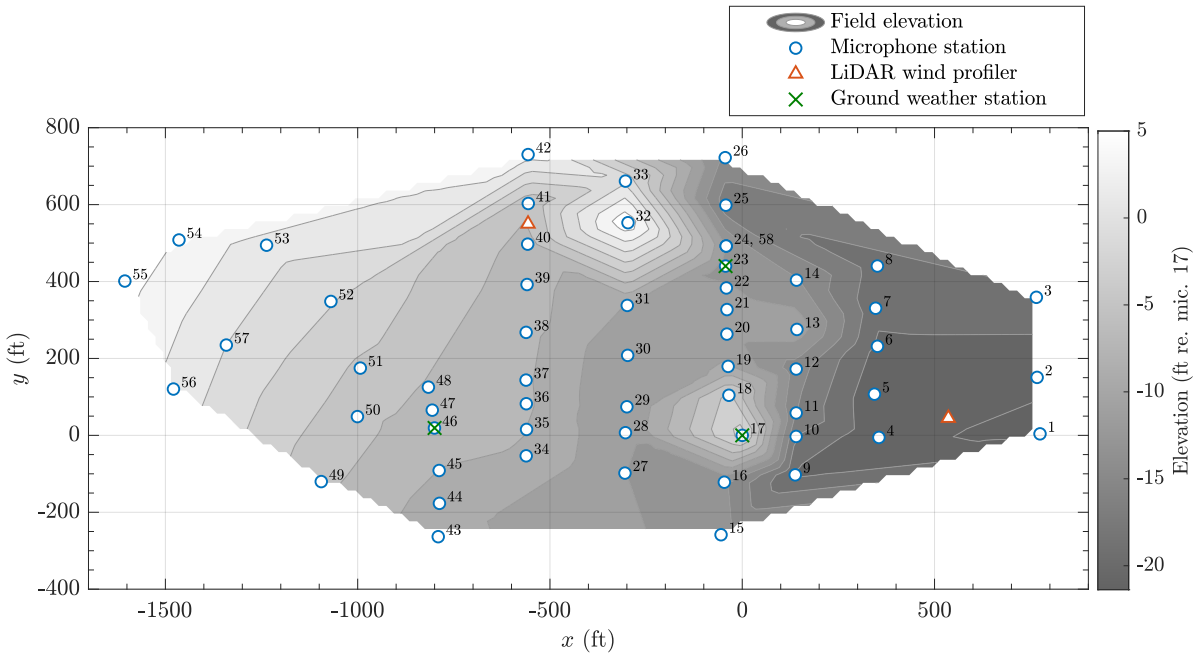

Figure 3. Distributed microphone array layout and weather measurement systems in the local coordinate system. Field elevation is also given in the contour.

Coordinated Time (UTC) to the data enabling synchronization of the acoustic signals across the array and with vehicle tracking and state data during postprocessing.

Microphones were calibrated at 250 Hz in the ground board using a specially designed adaptor and GRAS pistonphone. WAMS2 are radio controlled from the Mobile Acoustics Facility (MAF)[†] using a frequency-hopping spread spectrum scheme in the 902-926 MHz UHF band with 1 W effective radiated power. Tasks sent to the units included requesting information on system health (battery power and pressure, temperature, humidity inside the unit), and when to acquire acoustic data. Voltage levels and waveforms of a recorded time series were monitored occasionally to ensure data quality.

A set of weather measurements was recorded and monitored throughout the test. Two ZephIR 300 portable IEC 60825-1 Class 1 eye-safe LiDAR systems were deployed and operated during flight. The LiDAR systems measured wind speed and direction at 12 heights up to approximately 1000 feet Above Ground Level (AGL). These systems were placed in close proximity to the two main flight paths and provided wind characteristics at altitude. Additionally, three ground weather stations were distributed across the microphone array and were also monitored and logged. These ground weather measurements included wind speed, wind direction, pressure, temperature, and humidity. During postprocessing, atmospheric absorption of the acoustic signals is based on an average of these field measurements for each test point.

On board the vehicle, time-dependent GPS position and altitude were logged at a nominal sample rate of 100 S/s. Additionally, vehicle attitude, true airspeed, and individual propeller states (rotation rate, blade pitch, and nacelle tilt) were also recorded with time stamps that enable synchronization with the acoustic signals.

III.C. Test Point Conditions

Within the current capabilities of the vehicle, the test points covered representative conditions for all phases of flight. Over the course of six flight test days, more than 100 test points were flown at 31 unique conditions. Table 1 summarizes the test points and provides condition codes that will be discussed in this paper. Hover in ground effect and hover out of ground effect (Condition Code H) were conducted over the runway at WP2.

[†]see Ref. 14,15 for additional details on the MAF and supporting instrumentation

Departure profiles (Condition Code T in Table 1) were parameterized by flight path angle ($3° \leq \gamma \leq 5°$) and acceleration based on true airspeed (0.05 g $\leq a_\infty \leq$ 0.2 g), and captured transition from thrust-borne to wing-borne flight. Constant airspeed level flyovers (Condition Code L) were performed over a range of true airspeeds (50 kt $\leq V_\infty \leq$ 110 kt) at approximately 350 ft AGL, holding the nominal state for ± 2000 ft from the first and last microphone in the distributed array (not including the semicircular subarray surrounding the runway). Approaches (Condition Code A) were parameterized similar to the departures on flight path angle and acceleration ($-5° \leq \gamma \leq -3°$, -0.1 g $\leq a_\infty \leq -0.05$ g). Test points not covered in this paper include additional constant speed level flyovers, level flight acceleration and deceleration, and a small number of turning departures and approaches.

Table 1. Partial test matrix listing the flight conditions covered in this paper.

NASA Code	Condition Type	V_∞ (kt)	γ (deg.)	a_∞ (g)	Priority	No. of Runs	Route
A1	Approach	varies	-3	-0.05	1	3	Southern
A3	Approach	varies	-3	-0.1	1	7	Southern
A4	Approach	varies	-5	-0.05	1	4	Southern
H2	HIGE	0	0	0	1	2	WP2
H3	HIGE†	0	0	0	1	4	WP2
H6	HOGE	0	0	0	1	3	WP2
H7	HOGE‡	0	0	0	1	2	WP2
L2	Level Flyover	50	0	0	1	2	Northern
L3	Level Flyover	60	0	0	1	2	Northern
L7	Level Flyover§	100	0	0	1	6	Northern
L8	Level Flyover§	110	0	0	1	5	Northern
T1	Departure	varies	3	0.05	3	2	Southern
T2	Departure	varies	3	0.1	1	2	Southern
T3	Departure	varies	3	0.2	1	3	Southern
T4	Departure	varies	5	0.05	2	1	Southern
T5	Departure	varies	5	0.1	1	3	Southern
T6	Departure	varies	5	0.2	1	4	Southern

† *180° heading change relative to condition H2.*

‡ *180° heading change relative to condition H6.*

§ *Low propeller rotation rate.*

III.D. Wind Conditions

Generally speaking, the Joby aircraft may utilize differential thrust or control of propulsors to counteract wind or atmospheric turbulence to maintain a prescribed flight path and airspeed. The aeroacoustic source itself is also likely to be altered in the presence of turbulence or flowfield changes.[7] Due to the potential acoustic sensitivity of this vehicle class to varying winds, the goal was to fly under benign test conditions, e.g., <10 kt, to reduce propagation uncertainty and avoid large source noise changes, particularly given the immaturity of current research and understanding of AAM vehicle noise emissions. Fortunately, all test days were near ideal with winds averaging less than 3 kt at the ground and up to all working altitudes. Figure 4 shows the averaged wind velocity magnitude over both LiDAR units as a function of altitude for each test day over the period of time when testing occurred. Additionally, a 2σ bound, in which σ is the standard deviation, is also within the preferred range.

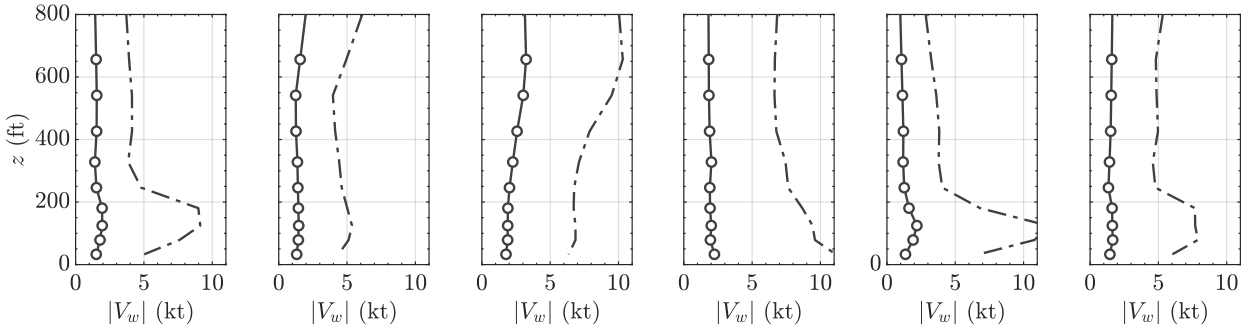

Figure 4. Day-averaged velocity magnitude wind profiles with 2σ bands (dotted lines), with day 1-6 from left to right. Each figure includes data from both LiDARs.

IV. Data Processing

IV.A. Ground Noise Contours

Measurements of the departure and approach conditions (Condition Code T and A, respectively) will be provided in the form of ground noise contours. The maximum A-weighted sound pressure level, $L_{A,\max}$, is computed at each microphone and is spatially interpolated to form the contours. In an effort to assess what would be heard at the ground, the only correction made to the data is the removal of the ground board pressure doubling effect. That is, the ground board is assumed to be sound-hard and independent of frequency and emission angle, e.g., $20\log_{10}(2)$=6.02 dB is uniformly subtracted from the measured data. Also, acoustic symmetry about a smoothed flight path has been assumed for visual purposes and to enable a representation of closed isoline contours. More specifically, data were acquired on the vehicle starboard side and mirrored to the port side. Evidence on the validity of assuming symmetry will be given in section VI.

IV.B. Level Flight Directivity Mapping

Acoustic directivity is computed for each level flight (Condition Code L) using a similar approach as the Acoustic Repropagation Tool (ART) methodology contained within the Advanced Acoustic Model (AAM), formerly the Rotorcraft Noise Model.[16,17] Figure 5 provides the vehicle-centered azimuth and elevation emission angle mapping that will be used to represent the data. While previous flight tests[18,19] from NASA have used the same general methodology, some internal modifications have been made that are not documented. Therefore, an overview of the process will be given here.

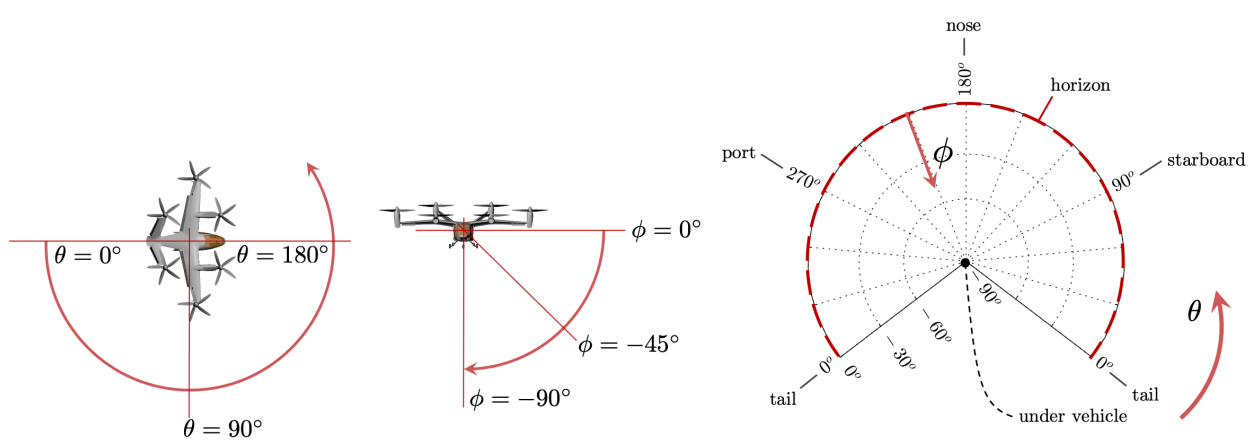

Figure 5. Definition of vehicle-fixed emission angles for mapping directivity.

The pressure time series at each ground microphone are first split into 0.5 second nonoverlapping data segments. For each segment, three power spectra are computed on 0.25 second blocks at 50% overlap using

a Hamming window. Ensemble averaging produces an independent spectral estimate for every 0.5 seconds. Prior to back propagation to the hemisphere surface, a number of steps are performed. To start, the spectral amplitude at each frequency for each narrowband spectrum estimate, per microphone, is compared to ambient levels recorded just prior to flight at that same frequency over its spectral-time history for a given run. Note that a 5% moving bandwidth average filter was applied to first smooth the ambient spectra. If the difference in those amplitudes is less than 3 dB, the data are removed due to poor signal-to-noise (SNR) ratio, to reduce back-propagating ambient noise. This criterion cannot always be met at higher frequencies due to the lower levels of radiated noise in this frequency range. Figure 6 shows an example illustrating the high frequency cutoff where the as-measured vehicle noise crosses the ambient + 3 dB line for one of the lowest SNR cases (110 kt level flyover, Condition Code L8). Under most circumstances, SNR was appropriate up to 5 kHz.

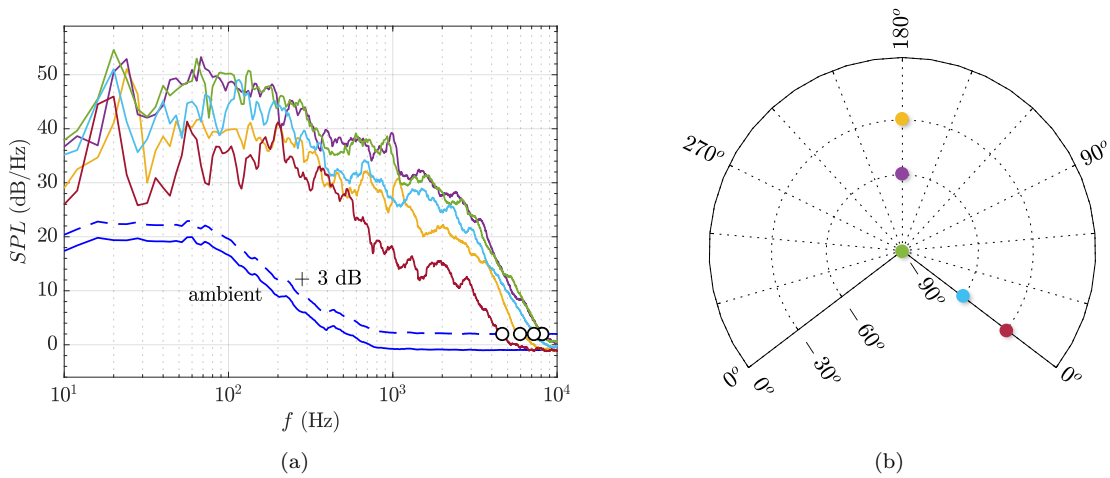

Figure 6. Spectral estimates used for directivity mapping for the 110 kt nominal true airspeed level flyover (Condition Code L8). The spectra in (a) are color coded based on emission angle as shown in (b). Ambient noise levels are also given, and the high frequency signal-to-noise cutoff is noted by the white filled circles.

Given the time-dependent vehicle position from the tracking data, the effects of the ground board, atmospheric absorption, and spherical spreading are removed. The pressure doubling effect is first removed as described in the previous section. Again following the ART methodology, the medium is assumed to be isotropic for atmospheric absorption. The ANSI S1.26[20] model is applied as a function of frequency given temperature, pressure, and humidity from an average of the weather station data.

Using the tracking data, these corrected narrowband spectra at each microphone are back-propagated (but not de-Dopplerized) to form an $r_0 = 100$ ft radius discretized source hemisphere centered at the onboard GPS receiver using straight rays between the observer and vehicle location at the time of emission. That is, the levels are adjusted by $20\log_{10}(r(\tau)/r_0)$, in which $r(\tau)$ is the distance between the vehicle and each microphone at the time of emission. Overall metrics (e.g., L, L_A, etc.) can then be computed by integrating the frequency spectra. Note that the frequency integration bounds of these metrics are set given the signal-to-noise ratio assessment in Figure 6. The directivity information will be given herein in the form of Lambert projections (i.e., Fig. 5) for minimal contour distortion.

V. Results

V.A. Departures and Approaches

A sample departure and approach test point will be provided to highlight, in general, characteristics of these events. Figure 7 provides an example ground noise contour of a departure event. During these test points, the vehicle took off from the ground and initiated a climbing acceleration over the microphone array. For the purposes of these noise contours, the acoustic data considered begin when the vehicle achieved a true airspeed of 2 kt. This was chosen as a reasonable compromise to obtain as much of the flown profile as possible without including any duration or acoustic differences during the finite hover just prior to forward

flight. The test point was deemed complete when the last row of microphones (stations 1-3) no longer had an appreciable signal-to-noise ratio over the frequencies of interest. The maximum A-weighted sound pressure level of each acoustic signal is interpolated between microphone stations to produce the contour. As expected, the peak $L_{A,\max}$ level is found near the takeoff location given the proximity of the vehicle to the microphones. Levels tend to be highest under the flight path and decrease in the lateral direction away from the flight path.

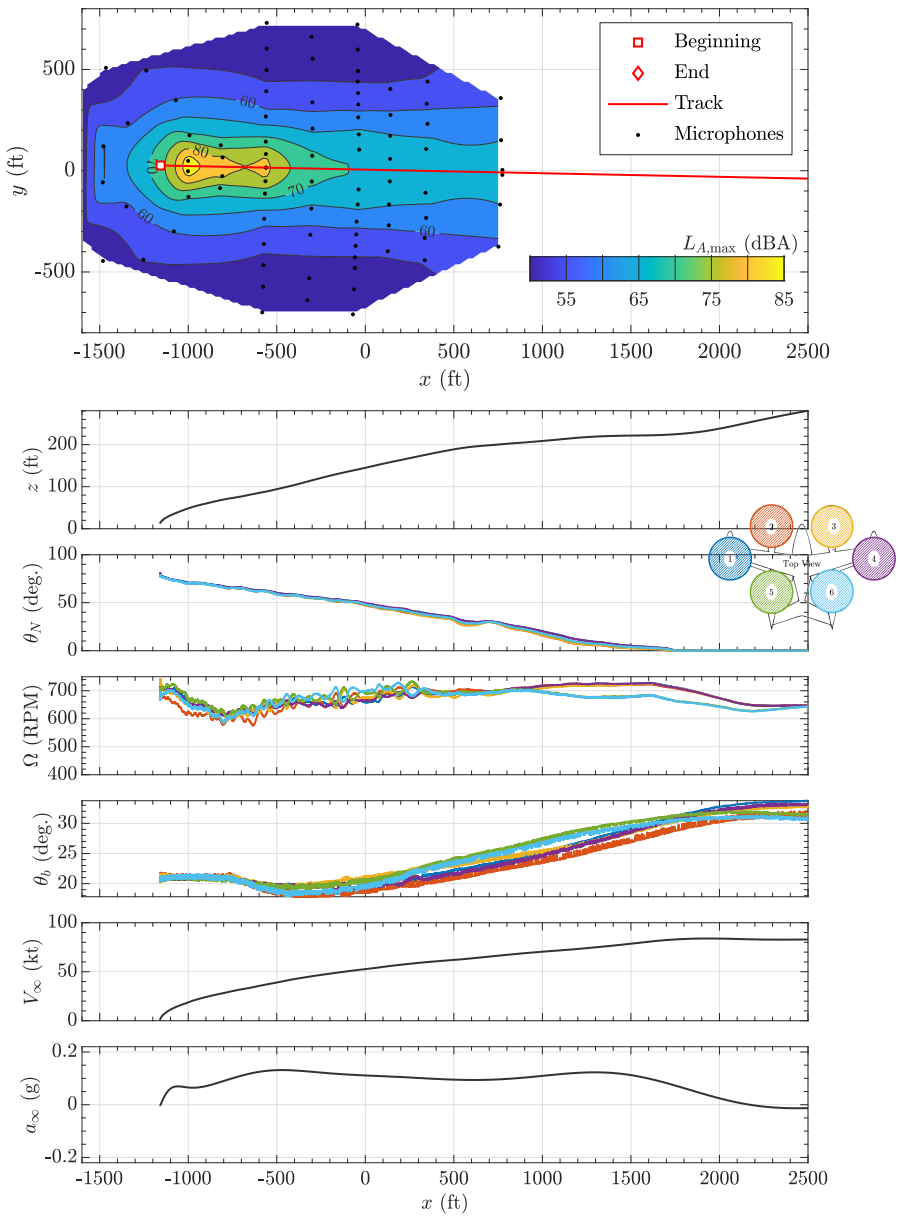

Figure 7. $L_{A,\max}$ **ground noise contour for a departure test point (Condition Code T5). Flight direction is left to right, and** $\overline{\gamma} = 3.6°$**,** $\overline{a}_\infty = 0.11$ **g. Propeller state data are color coded as provided in the vehicle inset.**

Also shown in Figure 7 are the vehicle altitude and state over the test point. The prescribed condition code was T5 with the intent to accelerate at 0.1 g at a flight path angle of 5°. To estimate the actual conditions flown, which may be slightly different than what was prescribed, the vehicle data were averaged between the times associated with the vehicle crossing $x = -800$ ft and when the vehicle reached 60 kt, accounting for the majority of the event. This criterion will be used subsequently in this section in an effort

to avoid beginning and ending effects, which sometimes involved pilot adjustments to get on condition. With this criterion and denoting the averaging scheme with a $\overline{(\cdot)}$, $\overline{\gamma} = 3.6°$ and $\overline{a}_\infty = 0.11$ g for Figure 7.

Nacelle angles of all six propellers change from near VTOL mode ($\theta_N = 90°$) to about 25° at the end of the array as the vehicle accelerates and transitions from thrust-borne to wing-borne flight. The transition rate occurs fairly quickly with a rate of change of nacelle angle of $-0.025°$/ft. Individual propeller rotation rates (Ω) and blade pitch (θ_b) are also given. The blade pitch and nacelle angles of each propeller changed uniformly and gradually over the test point and are representative of all departure test points. Rotation rate is found to be the least uniform and unsteady over the six propellers, although still within 100 RPM throughout the course of the departure test point. In addition to the gradual changes in rotation rate to execute the transition, small transient adjustments are continuously made by the unified flight controller to maintain the desired vehicle pitch, roll, and yaw. For the majority of propeller state traces, nominal settings are similar across all propellers. The exception to propeller state uniformity is found, in general, for accelerations 0.1 g or greater and when the vehicle is traveling at true airspeeds of approximately 70 kt or greater. Under these circumstances, the rotation rates of the tail propellers are reduced by about 50 RPM and blade pitch is increased relative to the wing-mounted propellers.

Figure 8 is an analogous set of plots to Figure 7 showing an example approach at $\overline{\gamma} = -4.7°$, $\overline{a}_\infty = -0.07$ g. As expected, similar contour features are found with respect to the flight path. Comparing this specific test point to the departure in Figure 7, the ground area encapsulated by any given level is markedly larger. Upon investigating the state data, the transition event is much more gradual relative to departure. For example, over the time that the vehicle is over the array, $\Delta\theta_N \approx 20°$ (versus 65° for the departure) with an approximate rate of change of 0.006°/ft. Additionally, the range of rotation rates is approximately 300 RPM, yielding much more variability as compared to departure. There is also a larger spread amongst individual propeller rotation rates during the deceleration, particularly at $-500 < x < 500$ ft. When inspecting acceleration for many of the approach test points, including this example, there are often deviations from the intended rate just prior to landing, i.e., $V_\infty < 20$ kt. The peak levels in ground noise contours may be sensitive to such rapid changes given the proximity of the microphones to these occurrences, although this sensitivity has not yet been investigated.

One of the major objectives of this test was to develop an initial understanding of the noise levels that may be present during near-vertiport operations as these phases of a mission may impact adjacent communities the greatest. Moreover, if noise sensitivity to flight conditions (or vehicle state) is known, flight profiles could be designed to minimize emissions. Previous work has shown improvements can be made with conventional rotorcraft using general guidelines on how to 'fly neighborly' based on a vehicle's operational envelope.[10,21] As a first look, ground noise contours were generated for all departures and approaches, and the 65 dBA isoline was extracted. The total ground areas enclosed by these isolines are computed and given in Fig. 9. While this isoline was fully captured laterally to the flight path, the isoline was closed based on the array extent (maximum 2,300 ft) in the flight direction. Figure 9(a) plots the ground areas as a function of flight path angle, while Fig. 9(b) plots the same data as a function of acceleration. The most salient feature of these plots is the fact that approach consistently yields much larger ground areas for the chosen metric, and in an averaged sense, the contour area is approximately twice as large. When plotted against flight path angle (Fig. 9(a)), there is no obvious trend in each respective phase of flight. However, Fig. 9(b) does display a reasonable trend with acceleration for departures, and perhaps a weak trend for approaches aside from a few outliers.

It is worth noting that this metric is not duration based, and thus, is independent of how quickly the vehicle completes the test point. Interestingly, analogous plots of sound exposure level (not shown here) display very similar trends. Thus, these results can be loosely interpreted as dependent on trajectory and source noise changes. For the former, however, independence of trajectory as shown in Fig. 9(a) implies source noise changes (possibly through differences in the transition event or vehicle state) dominate this trend with departure acceleration. If that is the case, performing the transition to/from VTOL from/to wing-borne flight in a quicker manner could aid in reducing noise. Again, these results may be muddled for approaches given potential ground area sensitivity to the last 10% segment of the approach in which deceleration varied most drastically relative to the prescribed condition. Although strong correlation with these flight condition parameters is not found, the large spread in ground area for each respective phase of flight indicates the potential for low-noise optimization of near-vertiport operations over the envelope tested here.

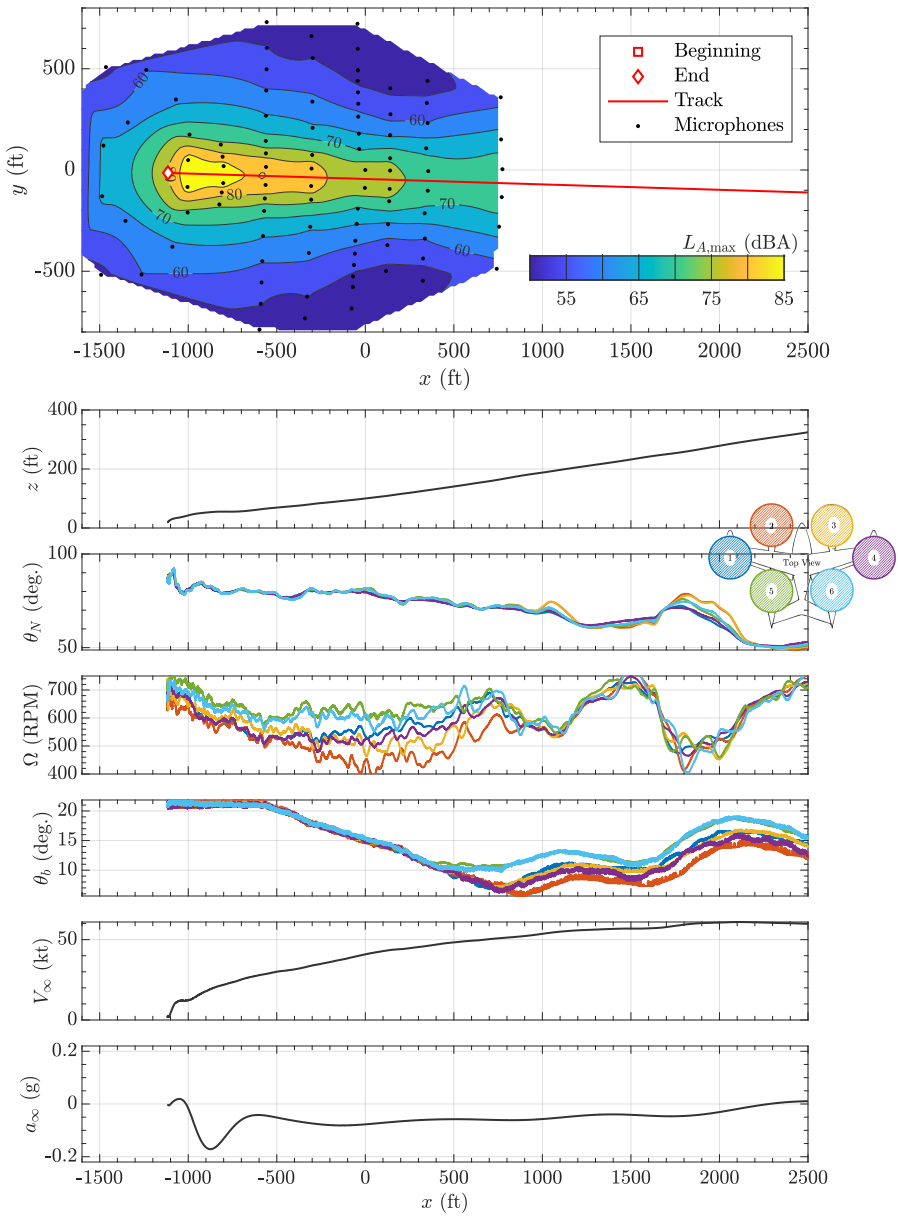

Figure 8. $L_{A,\max}$ **ground noise contour for an approach test point (Condition Code A4). Flight direction is right to left, and** $\overline{\gamma} = -4.7°$, $\overline{a}_\infty = -0.07$ **g. Propeller state data are color coded as provided in the vehicle inset.**

V.B. Level Flyovers

Directivities of constant true airspeed flyovers were mapped relative to the vehicle and averaged over the number of repeats for each condition. Figure 10 is an example at the average true airspeed $\overline{V}_\infty = 61$ kt (L3 in Table 1) over two flyovers. The vehicle was in semithrust-borne flight and, nominally, $\overline{\theta}_N = 47°$, $\overline{\Omega} = 651$ RPM. Note that while it is unlikely the vehicle will operate in this semithrust-borne flight mode for extended periods of time, maintaining this condition during overflight of the array enables full emission angle coverage of transition-like conditions. Similar to the ground noise contours in the previous section, symmetry has been assumed for visual purposes and applied about the 0-180° azimuth line. Unweighted and A-weighted integrated levels are provided in Figs. 10(a) and 10(b), respectively, and are scaled to a reference distance of 100 ft relative to the aircraft. These two metrics can be loosely thought of as a surrogate weighting scheme

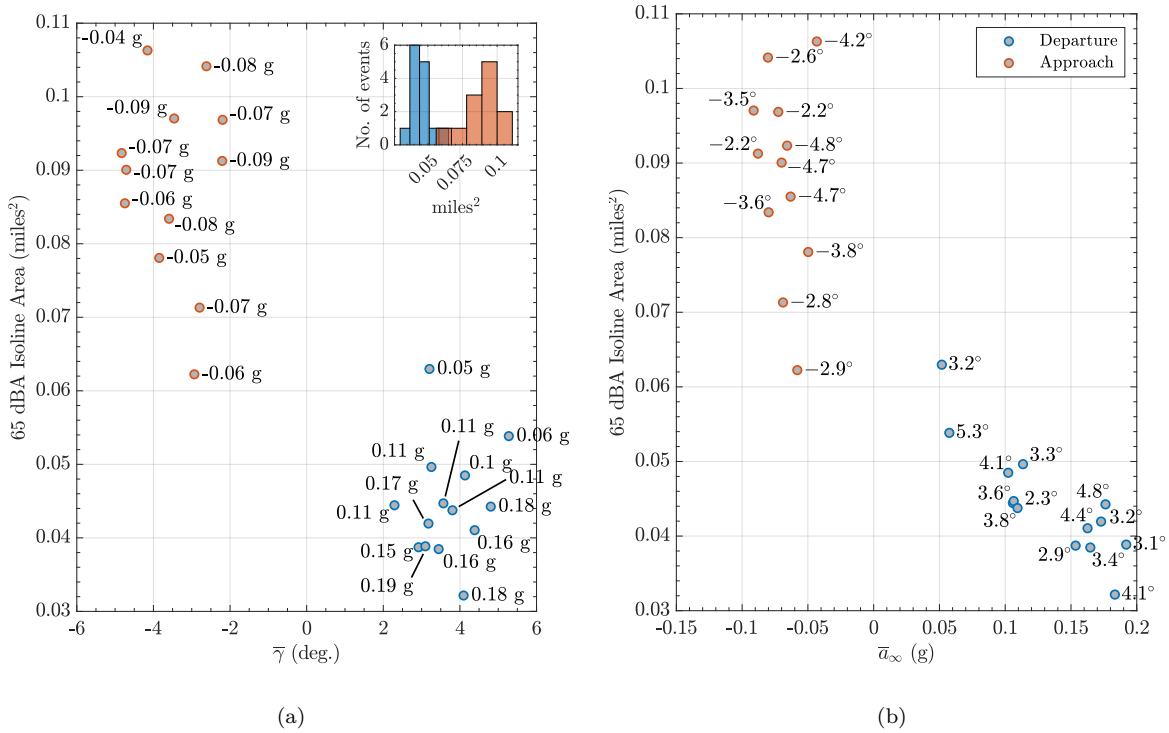

Figure 9. Variation of $L_{A,\max}$ 65 dBA isoline ground area with (a) average flight path angle and (b) acceleration. The inset figure is a histogram representation of the ground area.

between the low-frequency tonal content (e.g., blade passage frequencies) and higher frequency broadband noise. In most cases, particularly for semithrust-borne flight and hover, the unweighted low-frequency tonal content is higher in amplitude than the peak broadband levels.

The peak levels for both acoustic metrics are found under the vehicle and slightly aft ($\theta = 0°$, $\phi = -60°$), while the lowest levels are found to be in the front of the vehicle. A very different directivity pattern is found for full wing-borne flight as given in Fig. 11. For this condition, the average true airspeed was $\overline{V}_\infty = 103$ kt (L7 in Table 1) was acquired over six flyovers. With the assistance of the wing lift, the propellers are only required to produce forward thrust (i.e., $\overline{\theta}_N = 0.3°$) enabling a significant reduction in the nominal rotation rates to $\overline{\Omega} = 253$ RPM, which is more than 2.5 times lower than hover and semithrust-borne flight. Comparing this cruise-like condition to the 61 kt condition, maximum unweighted levels are lower by more than 6 dB. Two of the most important factors are the differences in rotation rate and nacelle angle. With the reduction in rotation rate and aligning the propellers with the flow direction, cruise flight is expected to be the quietest phase of flight within the tested envelope. When scaling these directivity plots to an observer distance of 1,640 ft (500 m), for example, the maximum unweighted and A-weighted levels are 53.4 dB and 45.2 dBA, respectively, in which the latter is consistent with previous measurements by Joby Aviation.[11] Note that higher cruise flight speeds may increase levels as the 110 kt flyover (L8) resulted in 1.1 dB and 1.3 dBA increases relative to the 103 kt (L7) flyover.

V.C. Hover

Figure 2 shows that the distributed microphone array featured a semicircular arrangement of seven microphones (stations 49-55) positioned near the runway. Hover test points (coded with 'H' in Table 1) were performed with the vehicle positioned at waypoint WP2 near the center of the semicircular array and toward the center of the distributed microphone array. This section focuses on the hover in ground effect (HIGE) and hover out of ground effect (HOGE) test conditions at WP2 (i.e., H2, H3, H6, H7). Multiple runs of each hover test condition were completed, but only one set are considered in the present work. The

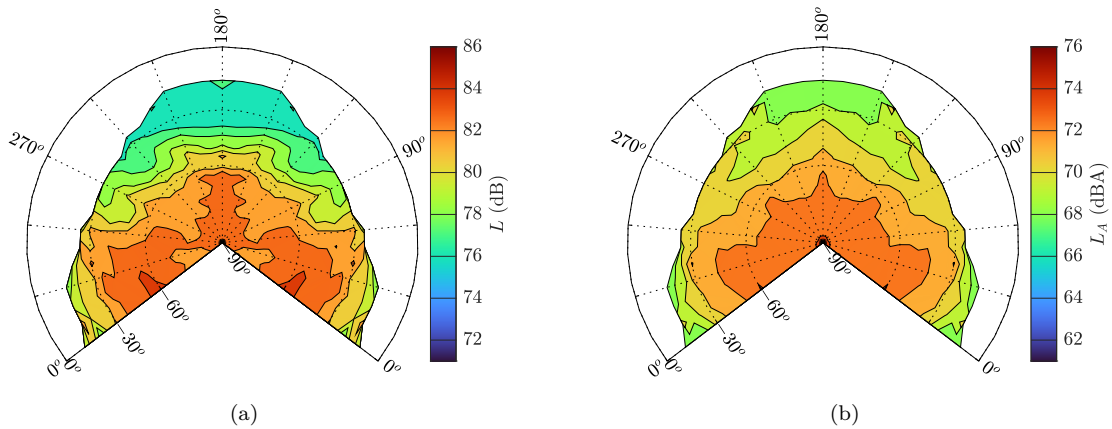

Figure 10. Averaged (a) overall and (b) A-weighted hemispheres over two flyovers in semithrust-borne flight at $\overline{V}_\infty = 61 \pm 2.1$ kt (L3 in Table 1), $\overline{\theta}_N = 47 \pm 5.1°$, $\overline{\Omega} = 651 \pm 66$ RPM. The range of each parameter is 2σ bounds over two flyovers. Levels are scaled to a reference distance of 100 ft.

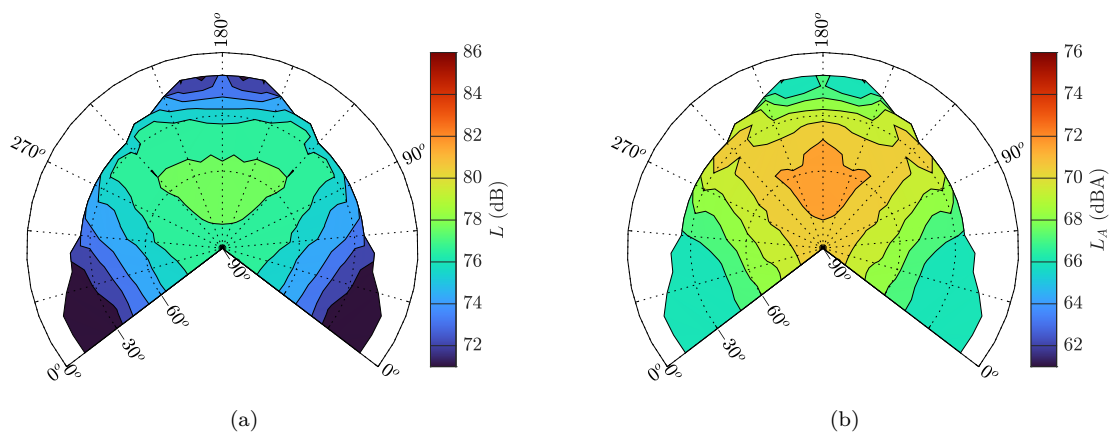

Figure 11. Averaged (a) overall and (b) A-weighted hemispheres over two flyovers in wing-borne flight at $\overline{V}_\infty = 103 \pm 0.9$ kt (L7 in Table 1), $\overline{\theta}_N = 0.3 \pm 0.1°$, $\overline{\Omega} = 253 \pm 12$ RPM. The range of each parameter is 2σ bounds over six flyovers. Levels are scaled to a reference distance of 100 ft.

test points were performed back-to-back over approximately 3.5 minutes, thereby avoiding large changes in environmental conditions.

After takeoff, the vehicle climbed to an altitude of approximately 38 ft AGL and navigated to WP2 to perform the H7 and H6 conditions. For these two HOGE conditions, the average elevation angle for the seven observers was approximately $\phi = -6°$ (below the vehicle horizon). The vehicle then descended to approximately 6 ft AGL to perform the H3 and H2 conditions before landing. For these two HIGE conditions, the average elevation angle for the seven observers was approximately $\phi = -1°$. For each of the four test conditions, the vehicle held trimmed conditions for approximately 30 s, but only 20 s of each run were used when processing the results shown in the present work.

Figure 12 shows four hover directivity plots. Figures 12(a) and 12(b) show integrated sound pressure level (L) in 5 dB increments while Figures 12(c) and 12(d) show A-weighted integrated sound pressure level (L_A) in 5 dBA increments. Consider Fig. 12(a), which shows unweighted levels for the two HOGE conditions. At each observer location, average levels were calculated by first determining the narrowband spectra for the

20 s of data used in each run, then applying propagation and atmospheric absorption corrections to scale to a reference observer distance of 350 ft (which is the nominal measurement distance), and finally integrating over 24 Hz $< f <$ 10 kHz. Note that no ground loss corrections were applied despite the observer angles being at grazing incidence.[22] It is expected that ground losses are fairly uniform over the various hover conditions; thus, comparison between these hover test points is reasonable. The minimum and maximum integrated levels were found by examining individual spectra averaged over 4 s segments using similar processing techniques. The black lines on the plots in Figure 12 are spline interpolations with a zero-slope constraint applied at the endpoints.

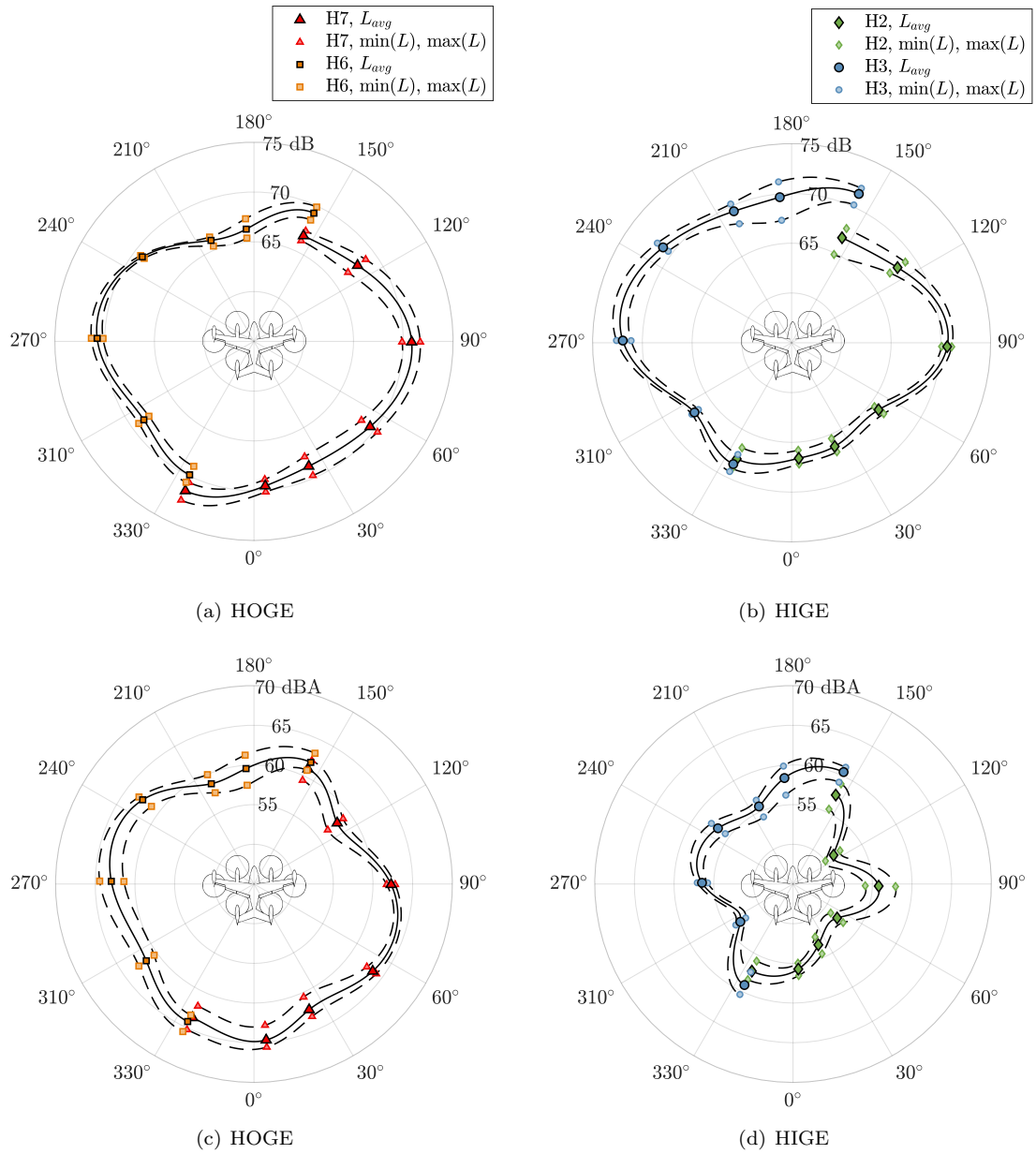

(a) HOGE (b) HIGE

(c) HOGE (d) HIGE

Figure 12. Hover directivity. Average levels (shown with larger markers) were determined using the spectra of pressure time histories scaled to a common reference observer distance of 350 ft and integrated over 24 Hz $< f <$ 10 kHz. Minimum and maximum levels (shown with smaller markers) were determined by examining 4 s segments of the 20 s of measured data used for each run. The black lines are spline interpolations through the processed results.

Returning to Figure 12(a), the overall directivity is generally constant across the rear half of the vehicle ($270° \leq \theta \leq 360°$ and $0° \leq \theta \leq 90°$). Levels are generally slightly lower in front of the vehicle ($90° \leq \theta \leq 270°$) compared to the rear. Some asymmetry is present when comparing the starboard ($0° \leq \theta \leq 180°$) and

port ($180° \leq \theta \leq 360°$) sides and, in particular, the levels near $\theta = 155°$ and $\theta = 335°$ are unequal for the two runs. Shifting attention to Figure 12(b), it can be seen that slight port/starboard asymmetry is also present for HIGE, and the difference in levels at $\theta = 155°$ is nearly 5 dB different for the two runs shown.

The disparity in levels for the same observer position in back-to-back runs is unexpected. In hover, the rotational speed and nacelle tilt of the six propellers are used to achieve a trimmed condition while blade pitch is relatively fixed. Table 2 lists the maximum drift of some of the vehicle state parameters during the four hover runs. Figure 13(a) shows the rotation rate and tip Mach number of the six propellers during the four hover runs. Consider propeller 3, located on the front of the vehicle on the starboard side, in which the average rotational speed was approximately 5% (30 RPM) greater for H3 than for H2. Assuming blade passage frequency levels scale with tip Mach number, this variation is not expected to produce a difference in levels by more than 1 dB. Figure 13(b) shows unweighted narrowband spectra for the observer at $\theta = 155°$ and confirms that the levels (specifically the tonal levels below 500 Hz) were indeed greater for H3. One potential reason for the difference could be from an aerodynamic interaction causing unsteady blade loading, particularly because unsteady loading noise can be dominant for low-tip-speed propellers.[23] However, further assessment is warranted to better understand the physical mechanisms at play.

Table 2. Maximum drift of vehicle state characteristics during the four hover runs considered. For the entries under *Propellers*, all six propellers were inspected to determine the maximum drift.

Position			Attitude			Propellers		
ΔX	ΔY	ΔZ	$\Delta\theta_{\text{roll}}$	$\Delta\theta_{\text{pitch}}$	$\Delta\theta_{\text{yaw}}$	$\Delta\Omega$	$\Delta\theta_b$	$\Delta\theta_N$
2.0 ft	4.6 ft	2.5 ft	2.7°	1.5°	1.5°	69 RPM	1.0°	3.1°

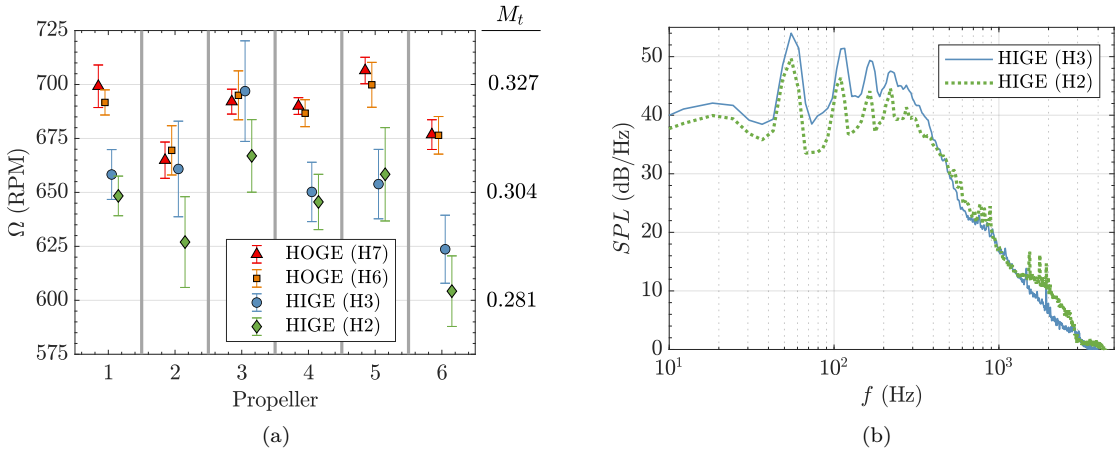

Figure 13. (a) Rotational speed of the six propellers during four hover runs. The markers show average values calculated over the 20 s of measured data used for each run while the bars show $\pm 2\sigma$. (b) Unweighted narrowband spectra for the observer located near $\theta = 155°$ based on 20 s of measured data per run.

It is also worth noting that the average altitude of the vehicle was 7.3 ft AGL for H3 whereas the altitude was 5.7 ft AGL for H2 (averaged over the 20 s of data considered in each run). Although this difference in altitude is less than 2 ft, when operating in ground effect, the rotational rates of the propellers required to achieve a trimmed state are more sensitive than when operating out of ground effect. This is illustrated by the bars in Figure 13(a) showing generally greater values of standard deviation for the two HIGE runs when compared to the bars for the two HOGE runs. The variability in rotation rates for the HIGE runs was potentially caused by unsteady propeller inflow and interactions between the airframe and flow near the ground, though flow measurements would be needed to better understand these phenomena.

Finally, when examining the directivity plots in Figure 12 more broadly, it can be seen that the variability in levels for each run is generally within 2 to 5 dB (or dBA) as illustrated with the smaller markers and dashed black lines. However, the levels and directivity patterns are sensitive to the trimmed vehicle state, which

introduces variability when comparing the two HIGE runs or two HOGE runs, despite the fact that the runs were performed back-to-back.

VI. Data Quality

In sections V.A and V.B, acoustic symmetry about the vehicle's longitudinal axis was assumed. This section will begin by investigating the validity of this assumption. Repeatability in acoustic levels as extracted from the directivity maps for level flyovers will then be presented.

VI.A. Acoustic Symmetry

With the vehicle position known, emission angles of microphones on both sides of the vehicle were first computed. Given the array size constraints, it was not possible to acquire data for emission angles that correspond to large lateral distances relative to the flight path. Thus, the comparison will be restricted to angles that are only moderately sideline of the flight path. Figure 14 provides integrated metrics over a full event for both a departure and an approach. Unweighted and A-weighted sound pressure level at 0.5 s increments are given for microphones with very similar emission angles as observed from both the vehicle port and starboard sides. Note that the data in this subsection are presented 'as measured' and are free of any corrections. The microphones chosen are different per figure, utilizing stations 15 and 20 for Fig. 14(a), and stations 45 and 48 for Fig. 14(b) (see Fig. 3 for microphone numbering). These microphone pairs were found to have the closest emission angle match to avoid directivity dependence. As shown, the integrated metrics are all within 2 dB of each other, with typical deviations even smaller. While not every test point can be compared in this way given the differences in observer angle, several additional test points also showed similar behavior. Divergence from symmetry mostly occurred when the spread of rotation rates over the propellers were the largest.

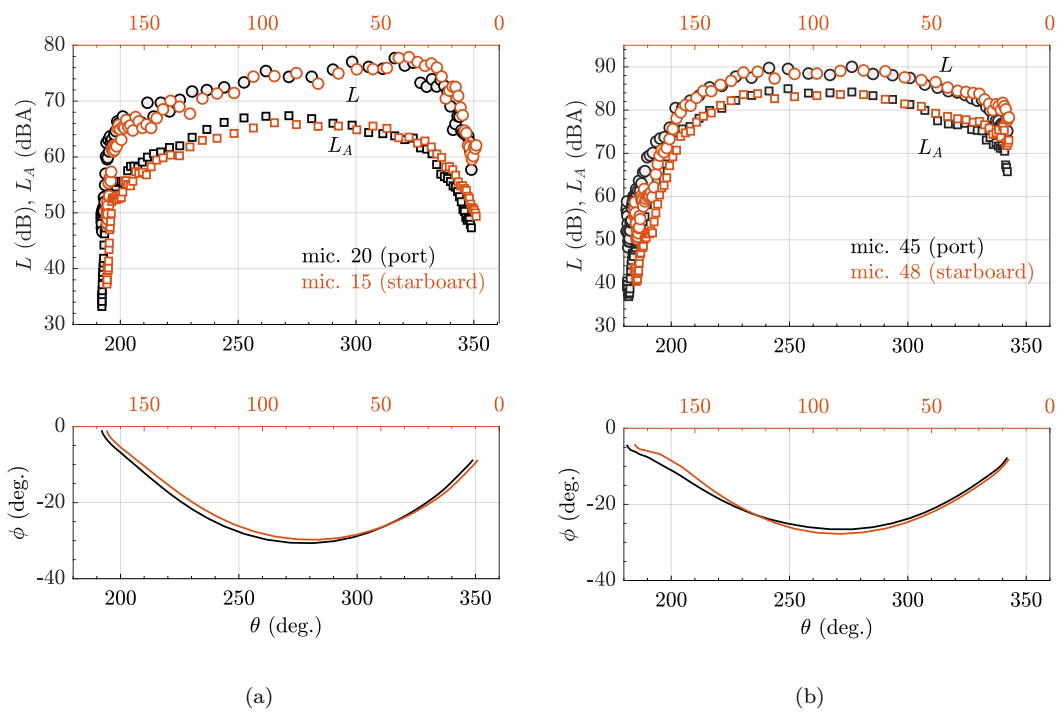

Figure 14. Longitudinal acoustic symmetry assessment of integrated metrics for a (a) departure (T5) and an (b) approach (A3).

Selecting a level flyover test point that yields the closest match between emission angles, the 50 kt flyover (Condition Code L2) is presented in Fig. 15. Integrated metrics of this condition follow suit with the previous figure in that differences are no more than 2 dB. However, it is useful to also look at spectral

agreement as a function of emission angle. Figures 15(a)-15(c) show spectra from 0.5 s 'instances' in time at matched emission angles. Each spectrum is color coded per Fig. 15(d) to visualize where these data fall on the directivity map. The spectra show very good agreement in overall levels and their frequency roll-off. Although, the tonal content at lower frequencies does show differences in amplitudes. Given these narrowband peaks are the blade passage frequencies, the expectation is that these amplitudes are unsteady and depend on the transient aerodynamic state (e.g., spread of rotation rates across the propellers) to maintain vehicle attitude and flight path. From this, symmetry is a reasonable assumption to characterize fixed nominal state directivity trends.

VI.B. Repeatability

While the previous section focused on comparing data acquired at the same instance in time, it is also worthwhile to understand the repeatability of acoustic levels over multiple test points at the same condition. As summarized in section V.C, further investigation is needed to understand repeatability and variation in levels for hover. Additionally, vehicle state data from repeated departure and approach test points were often too dissimilar to truly compare as repeated conditions. To this end, repeatability will be assessed only on the level flyovers. From inspection of the dataset, slightly larger differences were observed for the unweighted sound pressure level, and is thus the selected metric for this discussion. Figure 16 provides unweighted sound pressure levels extracted directly from the directivity maps shown in Figs. 10 and 11. For the lower airspeed case at 60 kt, two flyovers were performed on different days. The envelope of levels was extracted over these two flyovers for a constant elevation angle $\phi = -60°$ and plotted in Fig. 16(a) as a function of azimuth. Similarly, the higher airspeed case of 100 kt, as shown in Fig. 16(b), displays the envelope of levels of six flyovers at this condition, which were acquired over two days. In both conditions, the directivity and levels deviated by about 1-2 dB.

VII. Concluding Remarks

An extensive acoustic flight test was conducted by NASA and Joby Aviation on Joby Aviation's preproduction prototype vehicle through the AAM National Campaign Developmental Test (NC-DT). Ground-based acoustic measurements were gathered on representative conditions for all phases of flight. Postprocessing ensured signal-to-noise ratio was appropriate. Ground noise contours were computed for near-vertiport operations using the distributed microphone array. Ground areas of 65 dBA isolines provide initial insight into potential community impact of this vehicle within its current operating envelope. Approach conditions yield significantly greater isoline areas relative to departure over the test envelope, and on average are twice as large. Directivity maps display emission-angle dependent features during flyovers at constant airspeeds, including semithrust-borne (i.e., transition-like conditions) and full wing-borne modes. These data could be leveraged in future studies to validate toolchains and better understand vehicle state dependencies, at least at a fixed nominal state. At the 100 kt airspeed tested, the wing-borne mode produces overall unweighted levels more than 6 dB lower than the 60 kt semithrust-borne condition, which is largely accomplished by the 2.5 times reduction in propeller rotation rates. While it is unknown how levels will scale for airspeeds greater than 100 kt, cruise conditions flown in this test were found to be the quietest phase of flight. At a fixed elevation angle, azimuthal directivity of hover is found to have slight asymmetry and vary 2 to 5 dB at any given observer over a single run. Disparities in levels at the same observer location between back-to-back runs is also found and needs to be further investigated. Finally, acoustic symmetry about the longitudinal axis was validated for pertinent flight conditions, which effectively simulated an increase in lateral span of the array. Repeatability of the level flyovers over several test days was found to be within 1-2 dB, providing initial insight into directivity uncertainty.

Acknowledgments

Thanks to the members of the NASA Comprehensive Rotorcraft Acoustic Flight Test Team (CRAFTT): Keith Scudder and Jeffrey Davis. Joby Aviation are gratefully acknowledged in the execution of this challenging test under difficult circumstances. Starr Ginn and Michael Marston from the NASA Armstrong Flight Research Center and Susan Gorton and Charles Lunsford from the NASA Langley Research Center are also acknowledged for their planning efforts. We also appreciate and thank Faisal Omar and Michele Cencetti

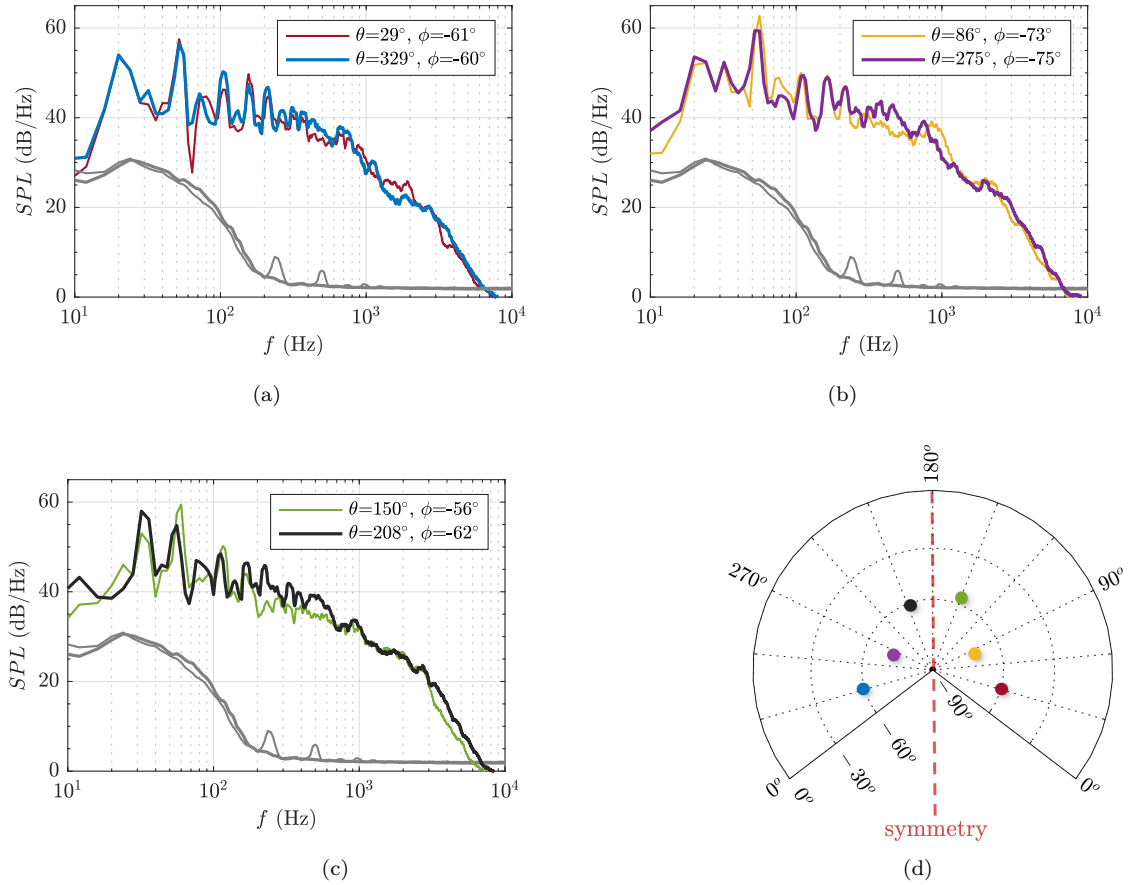

Figure 15. Longitudinal acoustic symmetry assessment of the acoustic spectra for a single level flyover at 50 kt (L2) (a) aft, (b) sideline, and (c) fore of the vehicle. The spectral lines are color coded based on observer angle as depicted in (d). Ambient levels given by the gray lines.

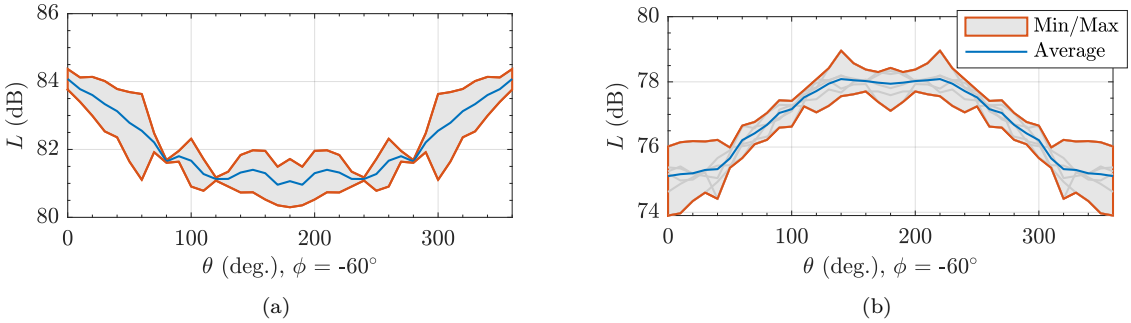

Figure 16. Sound pressure level envelope extracted from directivity plots for the full azimuth at $\phi = -60°$ at (a) 2 flyovers at 60 kt (L3) and (b) 6 flyovers at 100 kt (L7).

from the NASA Ames Research Center for the ADS-B real-time visualization dashboard used during the flight test. This work was supported by the NASA Aeronautics Research Mission Directorate, Revolutionary Vertical Lift Technology Project, with participation in the NASA National Campaign lead by the Advanced Air Mobility Project.

References

[1]"NASA Aeronautics Research Mission Directorate Strategic Implementation Plan," https://www.nasa.gov/aeroresearch/strategy, Accessed: 2021-1-5.

[2]"NASA Advanced Air Mobility National Campaign," https://www.nasa.gov/aamnationalcampaign/, Accessed: 2021-1-5.

[3]"Joby Aviation," https://www.jobyaviation.com/, Accessed: 2021-12-15.

[4]Zawodny, N., Christian, A., and Cabell, R., "A Summary of NASA Research Exploring the Acoustics of Small Unmanned Aerial Systems," *American Helicopter Society Specialists' Conference on Aeromechanics Design for Transformative Vertical Flight*, January 2018.

[5]Thurman, C., Zawodny, N., and Baeder, J., "Computational Prediction of Broadband Noise from a Representative Small Unmanned Aerial System Rotor," *76th Annual Forum of the Vertical Flight Society, Virtual*, 2020.

[6]Whelchel, J., Alexander, W. N., and Intaratep, N., "Propeller noise in confined anechoic and open environments," *AIAA Scitech 2020 Forum*, 2020, p. 1252.

[7]Fleming, J., Langford, M., Gold, J., Schwartz, K., Wisda, D., Alexander, N., and Whelchel, J., "Measured Acoustic Characteristics of Low Tip Speed eVTOL Rotors in Hover," *78th Annual Forum of the Vertical Flight Society*, 2020.

[8]Rizzi, S., Huff, D., Boyd, D., Bent, P., Henderson, B., Pascioni, K., Sargent, D., Josephson, D., Marsan, M., Hua, H., and Snider, R., "Urban Air Mobility Noise: Current Practice, Gaps, and Recommendations," NASA TP 2020-5007433, 2020.

[9]Bain, J., Mikić, G., and Stoll, A., "Aerodynamic And Acoustic Design Of The Joby Aviation eVTOL Propeller," *Vertical Flight Society 77th Annual Forum*, May 2021.

[10]Stephenson, J., Watts, M., Greenwood, E., and Pascioni, K., "Development and Validation of Generic Maneuvering Flight Noise Abatement Guidance for Helicopters," *Journal of the American Helicopter Society*, Vol. 67, No. 012012, 2022, pp. 1–12.

[11]Bain, J., Goetchius, G., and Josephson, D., "Flyover Noise Comparison Between Joby Aircraft and Similar Aircraft," *Vertical Flight Society 78th Annual Forum*, May 2022.

[12]Stoll, A. and Bevirt, J., "Development of eVTOL Aircraft For Urban Air Mobility At Joby Aviation," *Vertical Flight Society 78th Annual Forum*, May 2022.

[13]Denham, J., Krumenacker, J., D'Mello, G., and Lewis, M., "Taking advanced STOVL flight control to sea: The VAAC follow-on research programme," *American Helicopter Society Aerodynamics, Acoustics, and Test and Evaluation Technical Specialists Meeting*, 2002.

[14]Pascioni, K. A., Greenwood, E., Watts, M. E., Smith, C. D., and Stephenson, J. H., "Medium-Sized Helicopter Noise Abatement Flight Test," *Vertical Flight Society 76th Annual Forum*, October 2020.

[15]Pascioni, K., Greenwood, E., Watts, M., Smith, C., and Stephenson, J., "Medium-Sized Helicopter Noise Abatement Flight Test Data Report," NASA TM 20210011459, 2021.

[16]Page, J. A., Wilmer, C., Schultz, T., Plotkin, K. J., and Czech, J., "Advanced Acoustic Model Technical Reference and User Manual," WP-1304, SERDP, 2009.

[17]Conner, D., Burley, C., and Smith, C., "Flight Acoustic Testing and Data Acquisition for the Rotorcraft Noise Model (RNM)," *American Helicopter Society 62nd Annual Forum*, May 2006.

[18]Watts, M., Greenwood, E., Smith, C., Snider, R., and Conner, D., "Maneuver Acoustic Flight Test of the Bell 430 Helicopter Data Report," NASA TM 2014-218266, 2014.

[19]Watts, M., Greenwood, E., Smith, C., and Stephenson, J., "Noise Abatement Flight Test Data Report," NASA TM 2019-220264, 2019.

[20]"Method for the Calculation of the Absorption of Sound by the Atmosphere," Standard ANSI S1.26-1995, American National Standards Institute, Inc., New York, New York, 2004.

[21]Helicopter Association International Fly Neighborly Committee, *Fly Neighborly Guide*, Helicopter Association International, 2007.

[22]Anderson, M. C., Stephenson, J. H., Zawodny, N. S., and Gee, K. L., "Characterizing the effects of two ground-based outdoor microphone configurations," *Proceedings of Meetings on Acoustics*, Vol. 39, No. 1, 2019.

[23]Magliozzi, B., Hanson, D., and Amiet, R., "Propeller and Propfan Noise," *Aeroacoustics of Flight Vehicles: Theory and Practice*, Vol. 1, 1991, pp. 1–64.